

## First Principles Phase Diagram Calculations for the Octahedral-Interstitial System $\text{ZrO}_X$ , $0 \leq X \leq 1/2$

Benjamin Paul BURTON\*, Axel VAN DE WALLE<sup>1†</sup>, and Harold T. STOKES<sup>2‡</sup>

*Metallurgy Division National Institute of Standards and Technology,  
100 Bureau Drive, Gaithersburg, MD 20899, U.S.A.*

<sup>1</sup>*Engineering and Applied Science Division, California Institute of Technology,  
1200 E. California Blvd. MC 309-81, Pasadena, CA 91125, U.S.A.*

<sup>2</sup>*Department of Physics and Astronomy, Brigham Young University, Provo, UT 84602, U.S.A.*

(Received April 21, 2011; accepted November 8, 2011; published online December 19, 2011)

First principles based phase diagram calculations were performed for the octahedral-interstitial solid solution system  $\alpha\text{ZrO}_X$  ( $\alpha\text{Zr}[ ]_{1-X}\text{O}_X$ ;  $[ ] = \text{vacancy}$ ;  $0 \leq X \leq 1/2$ ). The cluster expansion method was used for ground state analysis, and to calculate the phase diagram. The predicted diagram has four ordered ground-states in the range  $0 \leq X \leq 1/2$ , but one of these, at  $X = 5/12$ , is predicted to disproportionate at  $T \approx 20$  K, well below the experimentally investigated range  $T \approx 420$  K. Thus, at  $T \gtrsim 420$  K, the first-principles based calculation predicts three ordered phases rather than the four that have been reported by experimentalists.

KEYWORDS:  $\text{ZrO}_X$ , Zr suboxides, zircalloy, first principles, phase diagram calculation, vacancy-interstitial ordering, order-disorder, alloy theory

### 1. Introduction

Zircalloy is used as nuclear fuel-rod cladding in light water reactors, but it is metastable with respect to oxidation by the  $\text{UO}_2$  fuel.<sup>1-4)</sup>

Oxidation of zircalloy transforms it from the high-temperature (high- $T$ ), oxygen-poor, bcc solution ( $\beta\text{Zr}_X$ ) into the low- $T$ , oxygen-rich, hcp-based solution ( $\alpha\text{ZrO}_X$ ). At temperatures between about 1173 and 573 K various ordered phases have been reported.<sup>5-13)</sup>

Octahedral interstitial ordering of oxygen (O), and vacancies ( $[ ]$ ) in  $\alpha\text{ZrO}_X$  ( $\alpha\text{Zr}[ ]_{1-X}\text{O}_X$ ,  $0 \leq X \leq 1/2$ ) increases microhardness<sup>14)</sup> and brittleness,<sup>1)</sup> and therefore, promotes stress corrosion cracking. Oxygen:vacancy (O: $[ ]$ ) order-disorder transitions were studied via heat capacity measurements: Arai and Hirabayashi<sup>12)</sup> examined alloys with O/Zr ratios of 0.16 and 0.24 at 473–973 K; Tsuji and Amaya<sup>15)</sup> made similar measurements on alloys with O/Zr ratios of 0.0, 0.10, 0.13, and 0.24, at 325–905 K.

Arai and Hirabayashi<sup>12)</sup> achieved a high degree of long-range O: $[ ]$ -order in samples that were cooled from 623 to 523 K, during a period of about one month, which indicates a high mobility of oxygen in  $\alpha\text{Zr}[ ]_{1-X}\text{O}_X$ , even at such modest temperatures; hence a system that is highly reactive even at such moderate temperatures.

A recent computational study<sup>16)</sup> reported ground-state structures and order-disorder transition temperatures for  $\text{Zr}_6\text{O}$  and  $\text{Zr}_3\text{O}$ , but did not present a calculated phase diagram, or report if the calculated order-disorder transitions in  $\text{Zr}_6\text{O}$  and  $\text{Zr}_3\text{O}$  are first-order, as experiment indicates, or continuous.

The results presented below are mostly consistent with experimental studies with respect to the comparison between computationally predicted ground-state (GS) structures and reported (experimental) low-temperature ( $T \lesssim 500$  K) ordered phases. With the exception that in the range  $0.25 \lesssim$

$X \lesssim 0.5$  the calculations predict only two ordered phases at  $T > 150$  K, rather than the three called  $\alpha'_2$ ,  $\alpha'_3$ , and  $\alpha'_4$  in Arai and Hirabayashi.<sup>12)</sup>

Experimental values for the maximum solubility of O in Zr,  $X_{\text{max}}$ , range from:  $X_{\text{max}} \approx 29$  at. %;<sup>6,17)</sup> to  $X_{\text{max}} \approx 35$  at. %;<sup>18)</sup> and  $X_{\text{max}} \approx 40$  at. %.<sup>10,12,13)</sup> The first-principles results presented here support a higher value; i.e.,  $X_{\text{max}} \geq 1/2$ . This may reflect an insufficiently negative calculated value for the formation energy of monoclinic  $\text{ZrO}_2$ .

### 2. Methodology

#### 2.1 Total energy calculations

Formation energies,  $\Delta E_f$  (Fig. 1) were calculated for fully relaxed hcp  $\alpha\text{Zr}$ , hcp  $\alpha\text{ZrO}$  (hcp  $\alpha\text{Zr}$  with all octahedral interstices occupied by O), and  $96 \alpha\text{Zr}[ ]_m\text{O}_n$  supercells of intermediate composition ( $m, n$  integers). All calculations were performed with the density functional theory (DFT) based Vienna *ab initio* simulation program (VASP, version 445<sup>19,20)</sup> using projector-augmented plane-wave pseudo-potentials, and the generalized gradient approximation for exchange and correlation energies. Electronic degrees of freedom were optimized with a conjugate gradient algorithm, and both cell constant and ionic positions were fully relaxed. Pseudopotential valence electron configurations were:  $\text{Zr}_{\text{sv}}$ :  $4s4p5s4d$ ;  $\text{O}_s$ :  $3s^23p^4$ .

Total energy calculations were converged with respect to k-point meshes by increasing the density of k-points for each structure until convergence. A 500 eV energy cutoff was used, in the “high precision” option which guarantees that *absolute* energies are converged to within a few meV/site (a few tenths of a kJ/site of exchangeable species; O,  $[ ]$ ). Residual forces were typically 0.02 eV or less.

Calculated formation energies,  $\Delta E_f$ , relative to a mechanical mixture of  $\alpha\text{Zr} + \alpha\text{ZrO}$ , for the  $96 \alpha\text{Zr}_{m+n}[ ]_m\text{O}_n$  supercells are plotted as solid circles in Fig. 1. Values of  $\Delta E_f$  are

$$\Delta E_f = \frac{E_{\text{Str}} - mE_{\alpha\text{Zr}} - nE_{\alpha\text{ZrO}}}{(m+n)}, \quad (1)$$

\*E-mail: benjamin.burton@nist.gov

†E-mail: avdw@caltech.edu

‡E-mail: stokesh@byu.edu

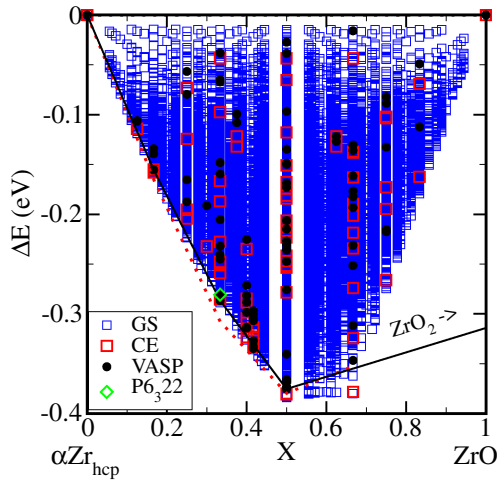


**Fig. 1.** (Color online) Comparison of VASP (solid circles) and CE (larger open squares, red online) formation energies,  $\Delta E_i$ , and a ground-state analysis on structures with 18 or fewer octahedral-interstitial sites (smaller open squares, blue online). Extension of the convex hull towards the formation energy of monoclinic zirconia,  $ZrO_2$ , indicates that the four ordered GS at  $X = 1/6, 1/3, 5/12,$  and  $1/2$  are also predicted to be GS of the Zr–O binary.

where:  $E_{Str}$  is the total energy of the  $\alpha Zr_{m+n} [ ]_m O_n$  supercell;  $E_{\alpha Zr}$  is the energy/atom of  $\alpha Zr$ ;  $E_{\alpha ZrO}$  is the energy/atom of  $\alpha ZrO$ .

### 2.2 The cluster expansion Hamiltonian

The cluster expansion, CE,<sup>21)</sup> is a compact representation of the configurational total energy. In the  $\alpha Zr [ ]_{1-x} O_x$  system, the solid solution configuration is described by pseudospin occupation variables  $\sigma_i$ , which take values  $\sigma_i = -1$  when site- $i$  is occupied by  $[ ]$  and  $\sigma_i = +1$  when site- $i$  is occupied by O.

The CE parameterizes the configurational energy, per exchangeable cation, as a polynomial in pseudospin occupation variables:

$$E(\sigma) = \sum_{\ell} m_{\ell} J_{\ell} \left\langle \prod_{i \in \ell'} \sigma_i \right\rangle \quad (2)$$

Cluster  $\ell$  is defined as a set of lattice sites. The sum is taken over all clusters  $\ell$  that are not symmetrically equivalent in the high-T structure space group, and the average is taken over all clusters  $\ell'$  that are symmetrically equivalent to  $\ell$ . Coefficients  $J_{\ell}$  are called effective cluster interactions, ECI, and the *multiplicity* of a cluster,  $m_{\ell}$ , is the number of symmetrically equivalent clusters, divided by the number of cation sites. The ECI are obtained by fitting a set of VASP FP calculated structure energies,  $\{E_{Str}\}$ . The resulting CE can be improved as necessary by increasing the number of clusters  $\ell$  and/or the number of  $E_{Str}$  used in the fit.

Fitting was performed with the Alloy Theoretic Automated Toolkit (ATAT)<sup>19,22–24)</sup> which automates most of the tasks associated with the construction of a CE Hamiltonian. A complete description of the algorithms underlying the code can be found in ref. 23. The zero- and point-cluster values were  $-0.421118$  and  $0.006221$  eV, respectively. The six pair and six 3-body ECI that comprise the complete CE Hamiltonian are plotted in Figs. 2(a) and 2(b), respectively. ECI for the isostructural  $TiO_x$  (open symbols, blue online)

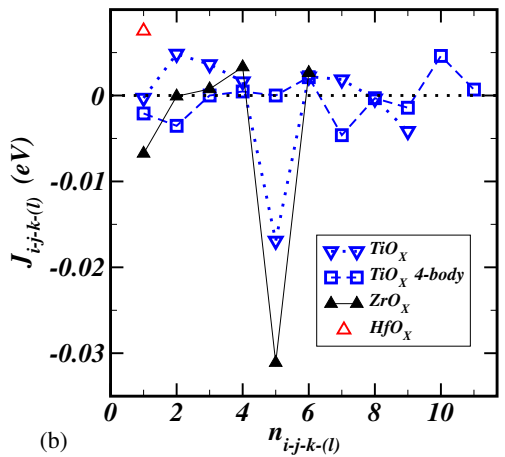
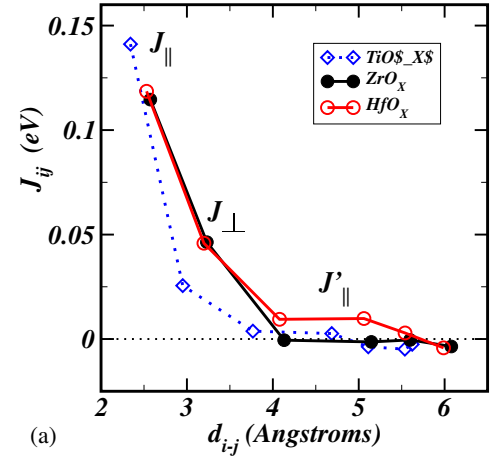


**Fig. 2.** (Color online) Effective Cluster Interactions (ECI) for pair and 3-body interactions. Solid black symbols indicate the  $ZrO_x$ -fit that was used in the phase diagram calculation reported here. Open diamonds and down-pointing triangles (blue online) indicate the results of a fit for the  $TiO_x$  system. Open circles and open up-pointing triangles (red online) are from a fit for the  $HfO_x$  system. (a) The first two pair-ECI are for nearest-neighbor O– $[ ]$  pairs that are parallel ( $J_{||}$ ) and perpendicular ( $J_{\perp}$ ), respectively, to  $c_{Hex}$ , and the fourth nn pair-ECI is the second-nn parallel to  $c_{Hex}$  ( $J'_{||}$ ). Pairwise-ECI are plotted as functions of inter-site separation. (b) 3-body interactions are plotted as functions of the index  $n_{i-j-k-(l)}$  which increases, nonlinearly, as the area of triangle  $i-j-k$  increases (4-body terms for the  $TiO_x$  system are also plotted; as open squares, blue online). Positive pairwise ECI imply a strong nn-pairwise O– $[ ]$  attraction, i.e., a strong nn-pairwise O–O repulsion.

and  $HfO_x$  (open symbols, red online) systems are also plotted for comparison. As expected, nearest neighbor (nn) O–O pairs are highly energetic, and therefore strongly avoided; hence nn-pair ECI are strongly *attractive* (ECI  $> 0$ , for O– $[ ]$  nn pairs); but beyond nn-pairs, the O– $[ ]$  pairwise ECI are close to zero. The ratio of magnitudes for nn-pair ECI that are parallel ( $J_{||}$ ) and perpendicular ( $J_{\perp}$ ) to  $c_{Hex}$ , respectively, is  $J_{||}/J_{\perp} \approx 2.5$ . Note that the fourth nn-pair ECI is the second-nn parallel to  $c_{Hex}$ , ( $J'_{||}$ ) and  $J'_{||}/J_{||} \approx 0.09$ .

The results presented here are similar to those in Ruban *et al.*<sup>16)</sup> although their effective pair interactions and ours are not identically defined.

Long-period superstructure (LPSS) phases were reported<sup>7,8)</sup> in samples with with bulk compositions close to  $Zr_3O$  (essentially the  $\alpha'_3$  field in Arai and Hirabayashi,<sup>12)</sup> their Fig. 9). Hence, it is reasonable to speculate that the CE-Hamiltonian might be like that in an axial next nearest

neighbor Ising model (ANNNI-model),<sup>25)</sup> in which one expects  $J_{\parallel}$  and  $J'_{\parallel}$  to be opposite in sign, and of comparable magnitudes ( $0.3 \lesssim -J'_{\parallel}/J_{\parallel} \lesssim 0.7$ <sup>25)</sup>); however,  $J'_{\parallel}/J_{\parallel} \approx 0.09$  (Fig. 2).

### 3. Results

#### 3.1 Ground-states

The CE was used for a ground-state (GS) analysis that included all configurations of [ ] and O in systems of 18 or fewer Zr-atoms (octahedral interstitial sites); a total of  $2^{18} = 262,144$  structures. Five GS were identified in the range,  $0 \leq X \leq 1/2$ , i.e., at  $X = 0, 1/6, 1/3, 5/12$ , and  $1/2$ ; solid circles (black online) on the convex hull (solid line) in Fig. 1. The extension of the convex hull towards monoclinic zirconia ( $\text{ZrO}_2$ ) is also plotted in Fig. 1. The CE-results suggest that all four VASP-GS in the  $\alpha\text{Zr}[\ ]_{1-X}\text{O}_X$  subsystem are also GS of the Zr–O binary, and that the maximum solubility of O in  $\alpha\text{Zr}_{\text{hcp}}$  is  $X_{\text{max}} \approx 1/2$  (higher than the experimental value,  $X \approx 0.4$ ). Note that, the predicted CE-GS at  $\text{Zr}_3\text{O}_2$  is not a GS for the VASP calculations (not a VASP-GS); hence the VASP-predicted maximum solubility of O in Zr is  $X_{\text{max}} \approx 0.5$ .

The larger open squares (red online) in Fig. 1 are CE-calculated values for the  $\Delta E_f$  that correspond to the VASP calculations, and the smaller open squares (blue online) are  $\Delta E_f$  for the remaining  $262,144 - 96 = 262,048$  structures in the GS analysis. The open diamond symbol (green online) indicates the calculated formation energy for the  $P6_322$  structure for  $\text{Zr}_3\text{O}$  that was originally proposed by Holmberg and Dagerhamn;<sup>5)</sup> this structure is also described in Table I. All space group determinations were performed with the FINDSYM program.<sup>19,26)</sup>

Crystal structures of the VASP- and CE-GS in Zr–ZrO are described in Table I and their idealized structures are drawn in Figs. 3(a)–3(d): Zr is represented by spheres connected with bond-sticks (yellowish-green online); O is represented by isolated spheres with bond-sticks (blue online); and [ ] are represented by isolated spheres (red online).

Various low-T ordered structures have been reported,<sup>6,8–13)</sup> with the most recent review by Sugizaki *et al.*;<sup>13)</sup> who used neutron diffraction to study short-range order in  $\text{ZrO}_{0.3}$  solid solutions. Their Figs. 1(a)–1(c) presented representations of three ordering schemes that were observed within different homogeneity ranges: (a)  $\text{ZrO}_x$  at  $X \lesssim 1/3$  ( $P321$ ); (b)  $\text{ZrO}_y$  at  $1/3 \lesssim X \lesssim 0.4$  ( $P6_322$ ); (c)  $\text{ZrO}_z$  near the solubility limit  $X \approx 0.4$  ( $P\bar{3}1m$ ). Space groups for these idealized structures were not reported by Sugizaki *et al.*;<sup>13)</sup> they were determined in this work with the FINDSYM program.<sup>26)</sup> Comparing structures (a)–(c) above to the results of this work: (a) VASP calculations indicate that this structure is clearly not a GS; (b) is the  $P6_322$  structure shown as an open diamond (green online) in Fig. 1, its formation energy is very close, but higher than, the VASP-GS at  $X = 1/3$ ; (c) is the same  $P\bar{3}1m$  structure as the VASP-GS at  $X = 1/2$ .

##### 3.1.1 $\text{Zr}_6\text{O}$ , $X = 1/6$ , $\alpha'_1$

The structure of  $\text{Zr}_6\text{O}$  is thought to be isomorphic to that of  $\text{Hf}_6\text{O}$  and  $\text{Ti}_6\text{O}$ .<sup>12,18)</sup>  $a \approx \sqrt{3}a_0$ ;  $c \approx c_0$ ;  $Z = 3$  ( $a_0$  and  $c_0$  are the cell constants of the disordered  $P6_3/mmc$  alloy).<sup>9)</sup> This is also the VASP-GS at  $X = 1/6$ , Fig. 3(a) and Table I.

**Table I.** Crystal structure parameters for predicted ground-state phases in the  $\alpha\text{Zr}[\ ]_{1-X}\text{O}_X$  system. Cell constants are given in Å.

System	X atomic fraction O	Space group IT number Pearson symbol	Calculated cell constants (Å)	Idealized atomic coordinates
$\text{Zr}_6\text{O}$	1/6	$R\bar{3}$ 148	$a \approx \sqrt{3}a_0$ $= 5.5333$	O: 1/6, 1/6, 1/6 Zr: 3/4, 1/12, 5/12
	1/7	hP7	$c \approx 3c_0 = 15.333$	Zr: 11/12, 7/12, 1/4 Zr: 1/12, 5/12, 3/4 Zr: 1/4, 11/12, 7/12 Zr: 5/12, 3/4, 1/12 Zr: 7/12, 1/4, 11/12
$\text{Zr}_3\text{O}$	1/3	$R\bar{3}c$ 167	$a \approx \sqrt{3}a_0$ $= 5.5671$	O: 1/6, 1/6, 1/6 O: 2/3, 2/3, 2/3
	1/4	hP8	$c \approx 3c_0 = 15.381$	Zr: 3/4, 1/12, 5/12 Zr: 11/12, 7/12, 1/4 Zr: 1/12, 5/12, 3/4 Zr: 1/4, 11/12, 7/12 Zr: 5/12, 3/4, 1/12 Zr: 7/12, 1/4, 11/12
$\text{Zr}_3\text{O}$	1/3	$P6_322$ 182	$a \approx \sqrt{3}a_0$ $= 5.5585$	O: 1/3, 2/3, 0 O: 2/3, 1/3, 1/2
	1/4	hP8	$c \approx c_0 = 5.1327$	Zr: 1/3, 0, 0 Zr: 0, 1/3, 0 Zr: 2/3, 2/3, 0 Zr: 2/3, 0, 1/2 Zr: 0, 2/3, 1/2 Zr: 1/3, 1/3, 1/2
$\text{Zr}_{12}\text{O}_5$	5/12	$R\bar{3}$ 148	$a \approx \sqrt{3}a_0$ $= 5.5568$	O: 1/12, 1/12, 1/12 O: 1/4, 1/4, 1/4
	5/17	hP17	$c \approx 3c_0 = 30.861$	O: 1/2, 1/2, 1/2 O: 2/3, 2/3, 2/3 O: 11/12, 11/12, 11/12 Zr: 1/8, 11/24, 19/24 Zr: 1/24, 17/24, 3/8 Zr: 23/24, 7/24, 5/8 Zr: 21/24, 13/24, 5/24 Zr: 19/24, 1/8, 11/24 Zr: 17/24, 3/8, 1/24 Zr: 5/8, 23/24, 7/24 Zr: 13/24, 5/24, 21/24 Zr: 11/24, 19/24, 1/8 Zr: 3/8, 1/24, 17/24 Zr: 7/24, 5/8, 23/24 Zr: 5/24, 7/8, 13/24
$\text{Zr}_2\text{O}$	1/2	$P\bar{3}1m$ 162	$a \approx \sqrt{3}a_0$ $= 5.5501$	0, 0, 0 O: 1/3, 2/3, 1/2
	1/3	hP9	$c \approx c_0 = 5.1572$	O: 2/3, 1/3, 1/2 Zr: 0, 1/3, 3/4 Zr: 1/3, 1/3, 1/4 Zr: 1/3, 0, 3/4 Zr: 2/3, 0, 1/4 Zr: 2/3, 2/3, 3/4 Zr: 0, 2/3, 1/4

##### 3.1.2 $\text{Zr}_3\text{O}$ , $X = 1/3$ , $\alpha''_2, \dots, \alpha''_3$

Based on X-ray diffraction studies, Holmberg and Dagerhamn<sup>5)</sup> proposed a  $P6_322$  structure (open diamond, green online, in Fig. 1) with  $a \approx \sqrt{3}a_0$  and  $c \approx c_0$  for a

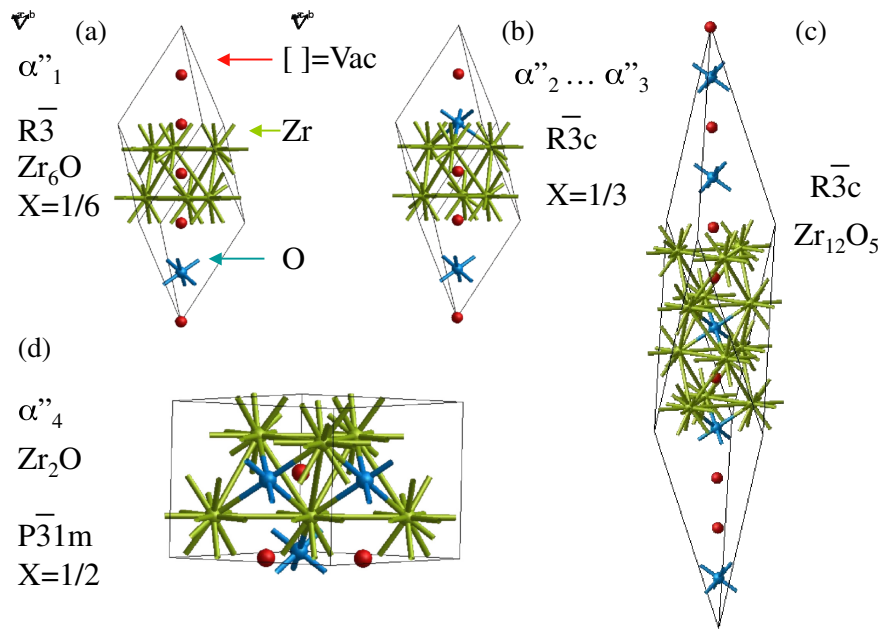


**Fig. 3.** (Color online) Idealized crystal structures of the four cluster-expansion-predicted suboxide ground-states: (a)  $\text{Zr}_6\text{O}$ ; (b)  $\text{Zr}_3\text{O}$ ; (c)  $\text{Zr}_{12}\text{O}_5$ ; (d)  $\text{Zr}_2\text{O}$ . Spheres connected by bond-sticks (yellowish-green online) represent Zr. Isolated spheres with bond-sticks (blue online) represent oxygen. Isolated spheres (red online) represent vacant octahedral sites.

sample with  $X \geq 0.26$ . Based on single crystal neutron diffraction studies Yamaguchi<sup>6)</sup> reported X-ray, electron and neutron diffraction data on samples in the range  $\text{ZrO}_{0.18}$ – $\text{ZrO}_{0.30}$  ( $1/5 \leq X \leq 3/7$ ) and listed atomic coordinates for a “ $P3c1$ ” structure with  $a \approx \sqrt{3}a_0$ ,  $c \approx 3c_0$ . Yamaguchi<sup>6)</sup> also reported confirmation of the  $P6_322$  structure in the composition range  $0.33 < X < 0.4$  ( $1/2 < X < 2/3$ ). The FP results presented here suggest that the VASP-GS at  $X = 1/3$  is the  $R3c$  structure depicted in Fig. 3(b). The calculated energy-difference between these two structures is only 0.006 eV, and this difference is probably within DFT error, but the precision of these calculations is sufficient to recognize the  $R3c$  structure as the VASP-GS.

### 3.1.3 $\text{Zr}_{12}\text{O}_5$ , $X = 5/17$

This structure does not correspond to any reported phase, and because it is predicted to disproportionate at  $T \geq 20$  K. It is not expected to be observed experimentally.

### 3.1.4 $\text{Zr}_2\text{O}$ , $X = 1/2$ , $\alpha''_4$

The only  $\text{Zr}_2\text{O}$  structure listed in Pearson<sup>27)</sup> is cubic, and the apparent solubility limit of  $X \approx 0.4$ , rather than  $X = 1/2$ , which suggests that the VASP calculations may underestimate the stability of monoclinic  $\text{ZrO}_2$ , and therefore finds the GS tieline between the  $P\bar{3}1m$  GS at  $X = 1/2$  and monoclinic  $\text{ZrO}_2$ , rather than between the  $R\bar{3}c$  GS at  $X = 1/3$  and monoclinic  $\text{ZrO}_2$ . Another possibility is that the experimentally measured low-temperature equilibrium between Zr-suboxides and monoclinic  $\text{ZrO}_2$  was measured at too low a fugacity of oxygen to stabilize the  $P\bar{3}1m$  phase at  $X = 1/2$ . As one expects from the ECI (Fig. 2), there are no O–O nn pairs in the VASP-GS  $P\bar{3}1m$  structure, or in any of the four structures with formation energies within 0.01 eV (right panel Fig. 1).

## 3.2 The phase diagram

A first principles phase diagram (FPPD) calculation was performed with grand canonical Monte Carlo (MC) simulations using the emc2 code which is part of the ATAT package.<sup>22–24)</sup> Input parameters for emc2 were: a simulation box with at least 1568 octahedral sites ( $15 \times 15 \times 6$  supercell); 2000 equilibration passes; 2000 Monte Carlo passes. The predicted phase diagram is shown in Fig. 4. Most phase boundaries were determined by following long-range order-parameters of the various ordered phases as functions of  $X$  and  $T$ . Here, long-range order parameters,  $\eta$ , are defined as the fraction of sites hosting O or [ ], relative to the corresponding fraction in the specified GS. Typically, but not always, these order parameters vary from unity in the perfectly ordered GS to zero in the disordered phase, and to different non-zero values in ordered phases other than their specified GS. Continuous or discontinuous changes in order parameters constrain and/or characterize phase boundaries. Dotted boundaries are used to acknowledge uncertainties in phase boundary determinations.

## 3.3 The intermediate temperature $\alpha'$ -phase

As observed experimentally in samples with  $X = 0.41$ ,<sup>10)</sup> (up-pointing triangles, green online, Fig. 4) a two-step order–disorder process is predicted for  $0.25 \lesssim X \lesssim 0.5$  (Fig. 5). The data reported in Hirabayashi *et al.*<sup>10)</sup> appear to indicate that both order–disorder transitions are second-order (continuous) in character, at least at  $X = 0.41$ , but the calculations reported here suggest that the lower-T transition is strongly first-order (at least at  $X = 1/2$ ) while the higher-T transition is continuous.

The simulated intermediate-temperature  $\alpha'$ -phase crystal structure was determined by symmetry analysis, using the ISODISTORT program.<sup>19,28)</sup> There are two plausible transi-

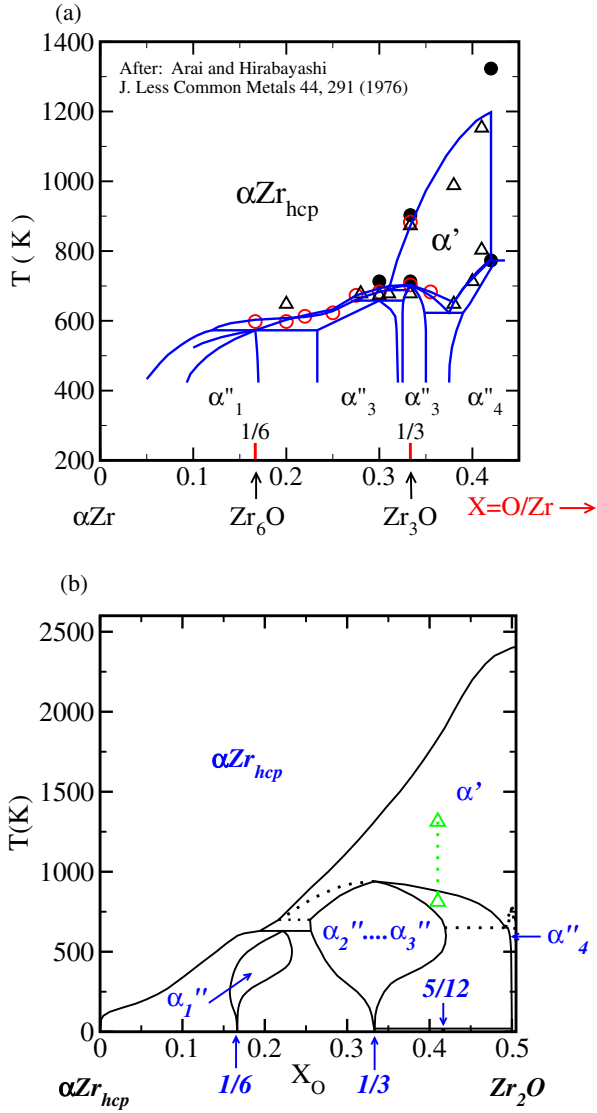


**Fig. 4.** (Color online) Comparison of experimental and calculated phase diagrams for the system  $\alpha\text{Zr}[1-X]\text{O}_X$ : (a) a combination of the “transformational diagram” (symbols) and the “tentative diagram” (solid lines) in Arai and Hirabayashi<sup>12)</sup> (their Figs. 1 and 9, respectively); (b) the diagram calculated from this work (dotted phase boundaries are less precisely determined than solid boundaries). Note the different results for  $0.25 \lesssim X \lesssim 0.42$  and  $420 \lesssim T \lesssim 725$  K.

tion paths from the  $P6_3/mmc$  high-T disordered phase to the  $P\bar{3}1m$  GS:

- (1)  $P6_3/mmc \rightarrow P6_3/mcm \rightarrow P\bar{3}1m$ ,  $K_1$  irreducible representation,  $(-1, -2, 0)$ ,  $(2, 1, 0)$ ,  $(0, 0, 1)$  basis;
- (2)  $P6_3/mmc \rightarrow P\bar{3}m1 \rightarrow P\bar{3}1m$ ,  $\Gamma_3^+$  irreducible representation,  $(0, -1, 0)$ ,  $(1, 1, 0)$ ,  $(0, 0, 1)$  basis.

Path (1) can be ruled out because it requires a first-order  $P6_3/mmc \rightarrow P6_3/mcm$  transition, with unit-cell expansion along both  $a_{\text{Hex}}$  axes; which neither experiment nor computation supports.

Path (2) permits a continuous  $P6_3/mmc \rightarrow P\bar{3}m1$  transition, as observed experimentally and supported computationally. The average  $\alpha'$ ,  $P\bar{3}m1$  structure is described in Table II and depicted in Fig. 6; where partially occupied O:[ ]-sites are represented by relatively smaller and larger spheres (blue online). The precise occupations of sites  $O_1$  and  $O_2$  can be written as  $\chi$  and  $2X - \chi$ , respectively; where

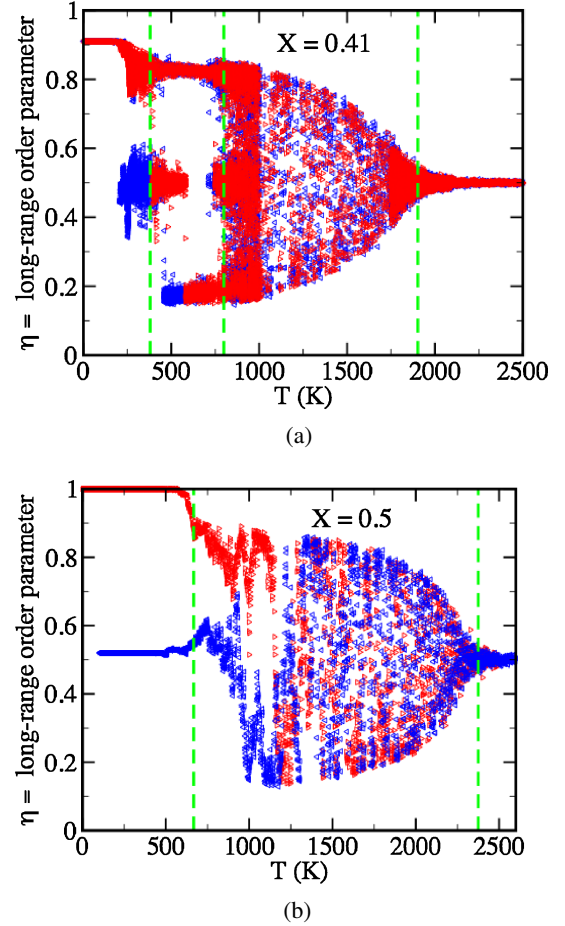


**Fig. 5.** (Color online) Calculated order-parameter vs temperature curves for: (a)  $X = 0.41$ ; (b)  $X = 1/2$ . Here, the long-range order parameter,  $\eta$ , is defined as the fraction of sites hosting oxygen (vacancies) as the corresponding sites in the specified ground state structure. Heating simulations are indicated by right-pointing triangles (red online) and cooling simulations are represented by left-pointing triangles (blue online). As observed experimentally, there is a two-step disordering process on heating.

**Table II.** Atomic positions in  $P\bar{3}m1$  (IT 164)  $\alpha'$  crystal structure:  $a \approx a_0 \approx 3.32 \text{ \AA}$ ;  $c \approx c_0 \approx 5.14000 \text{ \AA}$ ; \*  $X = \text{O/Zr}$ .

Atom	Wyckoff site	$x$	$y$	$z$	Occupancy
Zr	2d	1/3	2/3	$\approx 1/4$	1
$O_1$	1a	0	0	0	$x_{O1} < 1/2$
$O_2$	1b	0	0	1/2	$2X^* - x_{O1}$

$\chi < 1/2$  is the O-occupancy of site  $O_1$ , and  $X = \text{O/Zr}$ ; i.e., at  $X = 0.41$  and  $\chi = 0.22$  then  $2X - \chi = 0.60$ . With respect to space-group determination, the only requirement is that the occupancy of site- $O_1$  must differ from that of site- $O_2$ . The  $P\bar{3}m1$  structure is clearly consistent with the computational results shown in Figs. 7(a) and 7(b). For clarity, the O:[ ]-distributions (online O = red, [ ] = gray) in these figures were simulated on reduced ( $6 \times 6 \times 3$ ) supercells by cooling from 1000 to 900 K, and Zr-atoms were omitted. Note the strong preference for O:[ ]-ordering along  $c_{\text{Hex}}$ ; i.e., strong O–O nn avoidance along  $c_{\text{Hex}}$ . In the average  $P\bar{3}m1$  structure this leads to alternating nn-layers,  $\perp c_{\text{Hex}}$  that are relatively O-rich and O-poor ([ ]-rich). Visually, this statistical difference is obscured in the simulation

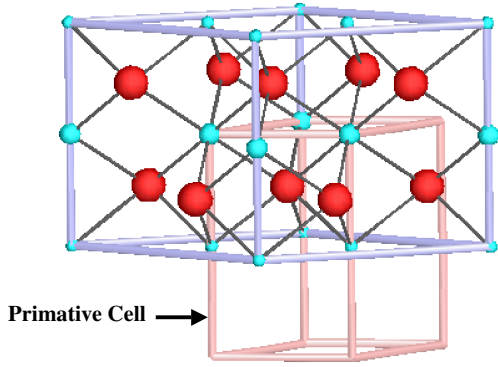
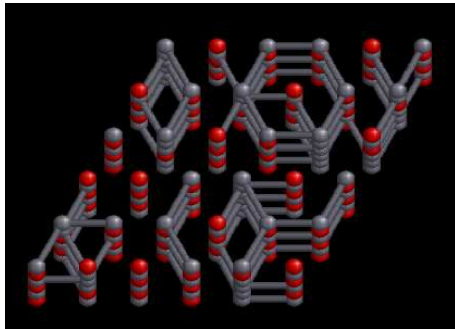
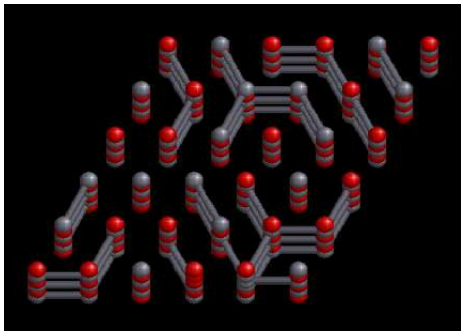


**Fig. 6.** (Color online) Average  $P\bar{3}m1$  structure of the  $\alpha'$ -phase. Small and intermediate sized spheres (blue online) represent less- and more oxygen-rich oxygen:vacancy-sites (O:[ ]-sites), respectively. Larger spheres (red online) represent Zr atoms. More and less O-rich O:[ ]-sites segregate into alternating layers perpendicular to  $c_{\text{Hex}}$ ; reflecting nearest neighbor O–O avoidance.



(a)



(b)

**Fig. 7.** (Color online) Simulated O-, [ ]-distributions (red: gray online, respectively) at: (a)  $X = 0.41$ ,  $T = 900$  K; and (b)  $X = 1/2$ ,  $T = 900$  K. For clarity, Zr-atoms are omitted and a reduced ( $6 \times 6 \times 3$ ) supercell were used. At  $X = 0.41$  no O–O nn pairs are evident parallel to  $c_{\text{Hex}}$ . At  $X = 1/2$ , almost all nn pairs parallel to  $c_{\text{Hex}}$  are O–[ ], although two columns (first row, columns 4 and 5) have some O–O nn pairs, while perpendicular to  $c_{\text{Hex}}$  there are many more O–O and [ ]–[ ] nn pairs.

snapshots [Figs. 7(a) and 7(b)] because one has: discrete O and [ ]; O:[ ]-disorder; and antiphase boundaries.

## 4. Discussion

### 4.1 Comparison of calculated and experimental phase diagrams

The main differences between the FPPD presented here and the “tentative phase diagram” in Arai and Hirabayashi<sup>12)</sup>

[Fig. 4(a); their Fig. 9] are with respect to their representations of broad homogeneity ranges for three ordered phases in the range  $0.25 \lesssim X \lesssim 0.42$  and  $420 \lesssim T \lesssim 725$  K. In this range, Arai and Hirabayashi report three low-T ordered phases,  $\alpha''_2$ ,  $\alpha''_3$ , and  $\alpha''_4$ ; whereas the FPPD has only two; note that the predicted GS at  $X = 5/12$  disproportionates at  $T \approx 20$  K. Also, the FPPD-predicted  $\alpha'$ -phase field is significantly larger than the corresponding field in Fig. 4(a), and at  $X = 0.41$  the  $\alpha' \rightleftharpoons \alpha\text{Zr}_{\text{hcp}}$  transition is predicted to occur  $\approx 500$  K higher than experiment suggests, Fig. 5(a). Typically, FPPD calculations overestimate order–disorder transition temperatures especially when, as here, the excess vibrational contribution to the free energy<sup>29,30)</sup> is ignored. This trend has been observed in numerous systems,<sup>30)</sup> although exceptions have been noted in systems where atomic size mismatch effects play a significant role;<sup>29)</sup> so it is not surprising that agreement between experiment and theory is not close for the  $\alpha' \rightleftharpoons \alpha\text{Zr}_{\text{hcp}}$  order–disorder transition. Note however, that the maximum temperatures for stabilities of phases other than  $\alpha'$  are roughly equal to those shown in Fig. 4(a).

### 4.2 Long-period superstructures at $X \approx 1/3$

Based on X-ray, neutron, and electron scattering data, Fehlmann *et al.*<sup>7)</sup> and Yamaguchi and Hirabayashi<sup>8)</sup> reported a variety of long-period superstructures (LPSS) in samples with bulk compositions  $X \approx 1/3$  [the  $\alpha''_3$  field, Fig. 4(a)] that were subjected to various heat treatments. The FPPD calculation presented here does not predict LPSS fields, but a similar calculation for  $\text{HfO}_X$  appears to predict Devil’s Staircases of ordered phases at  $\text{Hf}_3\text{O}$  and  $\text{Hf}_2\text{O}$ .<sup>31)</sup> In an ANNI-model like Hamiltonian, one expects,  $0.3 \lesssim -J'_{\parallel}/J_{\parallel} \lesssim 0.7$ , however, the 12-pair fit which includes  $J'_{\parallel}$  yields  $J_{\parallel}$  and  $J'_{\parallel}$  with the same sign and  $J'_{\parallel} \approx J_{\parallel}/10$ . Physically, the fitted values for  $J_{\parallel}$  and  $J_{\perp}$  are easy to rationalize in terms of O–O nn-repulsion, and this argues against stable LPSS phases, unless they are stabilized by competition between higher-order interactions; e.g., third and further nn-pair-ECI or multiplet interactions. In fact, FPPD calculations for the  $\text{HfO}_X$  system, which has a CE Hamiltonian very similar to that for  $\text{ZrO}_X$ , indicate a Devil’s Staircase of LPSS phases at  $\text{Hf}_3\text{O}$ .<sup>31)</sup>

## 5. Conclusions

Ground-state ordered phases are predicted at  $X = 0, 1/6, 1/3, 5/12$ , and  $1/2$ , but the one at  $X = 5/12$  is predicted to disproportionate at  $T \approx 20$  K, hence it is not expected to be observed experimentally. In the range  $0.25 \lesssim X \lesssim 0.5$ , in which Arai and Hirabayashi<sup>12)</sup> report three phases ( $\alpha''_2$ ,  $\alpha''_3$ , and  $\alpha''_4$ ) only two are predicted; i.e., the phase fields that Arai and Hirabayashi<sup>12)</sup> draw for  $\alpha''_2$  and  $\alpha''_3$  are predicted to be a single-phase solid solution. Figure 1(a) clearly indicates that a zeroth order model for octahedral interstitial O:[ ]-ordering is one in which first- and second-nn pairwise interactions ( $J_{\parallel}$  and  $J_{\perp}$ , respectively) strongly favor O–[ ] nn-pairs; i.e., O–O nn-pairs are highly unfavorable, and  $J_{\parallel}/J_{\perp} \approx 2.5$ . Including  $J'_{\parallel}$  in the ECI fit does not yield an ANNNI-like<sup>25)</sup> CE-Hamiltonian; however, recent FPPD calculations for the  $\text{HfO}_X$  system,<sup>31)</sup> (the  $\text{HfO}_X$ -CE is very similar to the  $\text{ZrO}_X$ -CE) predict Devil’s Staircases of LPSS phases at  $\text{Hf}_3\text{O}$  and  $\text{Hf}_2\text{O}$ .

The most probable transition path (on cooling) for O-rich solutions with  $X \gtrsim 0.4$ , is  $P6_3/mmc \rightarrow P\bar{3}m1 \rightarrow P\bar{3}1m$ ; hence the average  $\alpha'$ -structure has  $P\bar{3}m1$  symmetry with alternating O-rich and [ ]-rich layers  $\perp c_{\text{Hex}}$ .

- 1) A. W. Cronenberg and M. S. El-Genk: *J. Nucl. Mater.* **78** (1978) 390.
- 2) P. Hoffman and D. Kerwin-Peck: *J. Nucl. Mater.* **124** (1984) 80.
- 3) P. Hoffman, D. Kerwin-Peck, and P. Nikolopoulos: *J. Nucl. Mater.* **124** (1984) 114.
- 4) P. Hoffman and J. Spino: *J. Nucl. Mater.* **127** (1985) 205.
- 5) B. Holmberg and T. Dagerhamn: *Acta Chem. Scand.* **15** (1961) 919.
- 6) S. Yamaguchi: *J. Phys. Soc. Jpn.* **24** (1968) 855.
- 7) M. Fehlmann, A. Jostsons, and J. G. Napier: *Z. Kristallogr.* **129** (1969) 318.
- 8) S. Yamaguchi and M. Hirabayashi: *J. Appl. Crystallogr.* **3** (1970) 319.
- 9) M. Hirabayashi, S. Yamaguchi, and T. Arai: *J. Phys. Soc. Jpn.* **35** (1973) 473.
- 10) M. S. Hirabayashi, T. Yamaguchi, T. Arai, H. Asano, and S. Hashimoto: *Phys. Status Solidi A* **23** (1974) 331.
- 11) S. Hashimoto, H. Iwasaki, S. Ogawa, S. Yamaguchi, and M. Hirabayashi: *J. Appl. Crystallogr.* **7** (1974) 67.
- 12) T. Arai and M. Hirabayashi: *J. Less-Common Met.* **44** (1976) 291.
- 13) Y. Sugizaki, S. Yamaguchi, S. Hashimoto, M. Hirabayashi, and Y. Ishikawa: *J. Phys. Soc. Jpn.* **54** (1985) 2543.
- 14) A. Dubertret and P. Lehr: *C. R. Acad. Sci. (Paris)* **262** (1966) 1147.
- 15) T. Tsuji and M. Amaya: *J. Nucl. Mater.* **223** (1995) 33.
- 16) A. V. Ruban, V. I. Baykov, B. Johansson, V. V. Dmitriev, and M. S. Blanter: *Phys. Rev. B* **82** (2010) 134110.
- 17) R. F. Domagala and D. J. McPherson: *Trans. AIME* **200** (1954) 238.
- 18) J. P. Abriata, J. Gracés, and R. Versci: *Bull. Alloy Phase Diagrams* **7** (1986) 116.
- 19) Disclaimer: the use of a specific software package should not be misinterpreted as implying a NIST endorsement of that package.
- 20) G. Kresse and J. Hafner: *Phys. Rev. B* **47** (1993) 558; G. Kresse: Thesis, Technische Universität Wien (1993); G. Kresse and J. Hafner: *Phys. Rev. B* **49** (1994) 14251; G. Kresse and J. Furthmüller: *Comput. Mater. Sci.* **6** (1996) 15; G. Kresse and J. Furthmüller: *Phys. Rev. B* **54** (1996) 11169; cf. <http://tph.tuwien.ac.at/vasp/guide/vasp.html>.
- 21) J. M. Sanchez, F. Ducastelle, and D. Gratias: *Physica A* **128** (1984) 334.
- 22) A. van de Walle, M. Asta, and G. Ceder: *CALPHAD J.* **26** (2002) 539.
- 23) A. van de Walle and G. Ceder: *J. Phase Equilibria* **23** (2002) 348.
- 24) A. van de Walle and M. Asta: *Modelling Simulation Mater. Sci. Eng.* **10** (2002) 521.
- 25) P. Bak and J. von Boehm: *Phys. Rev. B* **21** (1980) 5297.
- 26) H. T. Stokes and D. M. Hatch: *J. Appl. Crystallogr.* **38** (2005) 237.
- 27) P. Villars and L. D. Calvert: *Pearson's Handbook of Crystallographic Data for Intermetallic Phases* (American Society for Metals, Metals Park, OH, 1985) Vol. 1.
- 28) B. J. Campbell, H. T. Stokes, D. E. Tanner, and D. M. Hatch: *J. Appl. Crystallogr.* **39** (2006) 607.
- 29) A. van de Walle and G. Ceder: *Phys. Rev. B* **61** (2000) 5972.
- 30) A. van de Walle and G. Ceder: *Rev. Mod. Phys.* **74** (2002) 11; A. van de Walle and G. Ceder: *J. Phase Equilibria* **23** (2002) 348; A. van de Walle, M. Asta, and G. Ceder: *CALPHAD J.* **26** (2002) 539; A. van de Walle and M. Asta: *Modelling Simulation Mater. Sci. Eng.* **10** (2002) 521.
- 31) B. P. Burton and A. van de Walle: arXiv:1107.4318; submitted to *CALPHAD J.*